AGU ADVANCING EARTH AND SPACE SCIENCE

JGR Solid Earth

Key Points:
- Deformation and fault zone development is driven by a complex interplay between compactant (C-type) and dilatant (T-type) regions
- Fracture growth is characterized by periodic cycles of coalescence
- C- and S-type events are consistent with a quasi-static premonitory phase, or foreshock, prior to failure plane localization

Source Mechanisms of Laboratory Earthquakes During Fault Nucleation and Formation

Thomas King[1,2] , **Sergio Vinciguerra[1]** , **Jodi Burgess[3]** , **Philip Benson[3]** , **and Luca De Siena[4,5]**

[1]Department of Earth Sciences, University of Turin, Turin, Italy, [2]Istituto Nazionale di Geofisica e Vulcanologia, Sezione di Catania - Osservatorio Etneo, Catania, Italy, [3]Rock Mechanics Laboratory, School of Earth and Environmental Sciences, University of Portsmouth, Portsmouth, UK, [4]Institute of Geosciences, Johannes Gutenberg University, Mainz, Germany, [5]Department of Geology and Petroleum Geology, School of Geosciences, King's College, University of Aberdeen, Aberdeen, UK

Abstract Identifying deformation and pre-failure mechanisms preceding faulting is key for fault mechanics and for interpreting precursors to fault rupture. This study presents the results of a new and robust derivation of first motion polarity focal mechanism solutions (FMS) applied to acoustic emission (AE). FMS are solved using a least squares minimization of the fit between projected polarity measurements and the deviatoric stress field induced by dilatational (T-type), shearing (S-type), and compressional (C-type) sources. 4×10 cm cylindrical samples of Alzo Granite (AG, porosity <1%) and Darley Dale Sandstone (DDS, porosity ≈14%) underwent conventional triaxial tests in order to investigate the relationships between increasing confining pressure (5, 10, 20, and 40 MPa), deformation and failure mode, and role of microstructural features. Results highlight that S-type events occur in very low numbers with poor spatial correlation to fault structure. Instead, deformation is driven by a complex interplay between compactant (C-type) and dilatant (T-type) regions of deformation. C-type events are the earliest precursor related to crack nucleation and T-type events mark new cracks opening, with the onset of fracture growth characterized by periodic cycles of coalescence. For AG a single sequence is able to lead to dynamic failure, while for DDS several cycles are needed for coalescence to take place due to the competition between dilatant and compactant deforming regions induced by multiple fracture nucleation sites. The occurrence of C- and S-type events is also consistent with a quasi-static premonitory phase, or foreshock, before a critical nucleation length allows the development of a planar localization.

1. Introduction

Seismic data provides key information on the physics of the fracture process ranging from fracture nucleation, crack growth, and damage accumulation, to crack coalescence and strain localization. Several micromechanical models have been developed over the years which seek to describe failure modes (e.g., Ashby & Hallam, 1986; Kemeny & Cook, 1991), taking into account pore-emanant fracturing (Baud et al., 2014), sliding wing cracks (Baud et al., 2014), friction effects (McClintock, 1962), and pore collapse (Zhu et al., 2010). To link these models to geophysical signatures recorded at the field scale, controlled laboratory rock deformation experiments equipped with dense microseismic arrays have become a routinely used tool (e.g., Benson et al., 2007; Fazio et al., 2017; Lockner et al., 1992). Here, fault growth may be considered analogous to the field scale development of earthquake rupture generating acoustic emission (AE), which is a well-used analog to tectonic earthquakes due to the scale invariance of these processes (Hanks, 1992; Hatton et al., 1994; Hudson & Kennett, 1981). The inclusion of AE sensors is now a routine laboratory rock physics method in the investigation of fault zone structure with the added benefit of a controlled environment.

There is an extensive literature reporting the evolution of fracture mechanisms inferred from the analysis of AE (e.g., tensile, shear, or compaction) that occur as damage propagates (e.g., Stanchits et al., 2006; Zang et al., 1998). Triaxial rock deformation experiments on fine-grained granites suggest that this process is tensile dominated (Cox & Scholz, 1988), whereas a higher proportion of shear-components are found in coarser-grained materials (Lei et al., 1992). This hypothesis is further supported by new observations linking macroscopic shear fracture to microcrack development prior to the yield point (Lei et al., 2000), highlighting the occurrence of tensile fracturing at the front of a shear process zone. These scenarios can

Table 1
Summary of Laboratory Acquisition Parameters

Characteristic	Value
Experimental conditions	
Confining pressure	5, 10, 20, and 40 MPa
Deformation rate	3.6 mm/hr
Sample dimensions	40×100 mm
Sample shape	Cylinder
Data acquisition	
Sensor model	PAC Nano30
Frequency sensitivity	1 MHz
Flat frequency response	125–750 KHz
No. of sensors	12
Trigger voltage	100 mV
Preamplifier	40 dB

be described as either strongly cohesive, where intergranular boundaries have little impact, or weakly cohesive, where such boundaries are easily ruptured by applied stresses (Baud et al., 2014).

The fracturing process is often described as a series of localized clusters of "damage" that accumulate through time (Kádár et al., 2020). These nucleating fractures amplify local stress concentrations, allowing for new fractures to further develop and grow in proximity. Furthermore, pre-existing flaws such cracks and pores concentrate stress, further promoting the development of a shear plane (Healy et al., 2006; McBeck et al., 2019). This "excitation" of fault growth, where the propagation of fractures encourages the development of secondary cracks in the vicinity is an important aspect of fault zone formation (Chen et al., 2014). The density and distribution of initial flaws, which control material cohesion and the elastic strain in the lead-up to failure, thus plays a critical role in determining when and how a rock will fail.

The aim of this study is to identify damage indicators in the fracture development process by mapping rupture source mechanisms (tensile, shear, and collapse) derived from microseismic signatures (AE) recorded during conventional triaxial deformation experiments. Two lithologies, representing end members in terms of rock physical properties (e.g., fabric, porosity, grain size, and cementation), were used: Alzo Granite (AG), Italy and Darley Dale Sandstone (DDS), UK. Unlike the commonly used average polarity method (e.g., Stanchits et al., 2006) the approach reported here uses the source radiation pattern (Finck et al., 2003; Kwiatek & Ben-Zion, 2013) to categorize events and obtain source orientations of mixed-mode type mechanisms.

2. Data and Methods

2.1. Materials Investigated and Sample Preparation

Alzo granite (AG) is typical of the white granites found in North-Western Italy. It is a medium-grained, plutonic rock comprising quartz, feldspar, and a high biotite content. Crystal sizes range between 2.5 and 6 mm for the biotite and 4–9 mm for the quartz and feldspars. Porosity (water immersion method) values are characteristically low at 0.72% ± 0.1% (Bugini et al., 2000). Cavallo et al. (2004) report an unconfined compressive strength of 229 MPa. Conversely, DDS from the quarry of Darley Dale, Derbyshire, UK is a brown-yellow, feldspathic sandstone with a modal composition of quartz (69%), feldspars (26%), clay (3%), and mica (2%). Previous studies report a connected porosity (water immersion method) of 13.3% ± 0.8% with grain sizes varying from 100 to 800 μm (Heap et al., 2009; Zhu & Wong, 1997). The unconfined compressive strength is ~160 MPa (Baud & Meredith, 1997). At the scale analyzed here, no distinct layering or laminations were present. Cylindrical rock samples were cored using a diamond tipped hollow coring drill to prepare 40 mm diameter samples that were then trimmed to 100 mm length with a diamond saw. End faces are accurately ground using a lathe fitted with a cross-cutting diamond grinding disk with surfaces flat and parallel to within 0.01 mm.

2.2. Laboratory Methods

Experiments were undertaken using a conventional triaxial apparatus (Sanchez Technologies), installed at the University of Portsmouth, UK (Benson et al., 2019). Laboratory acquisition parameters are summarized in Table 1. The apparatus is designed to deform cylindrical samples of 40×100 mm specimens at confining pressures of up to 100 MPa. A high flash-point oil (270°C) is used as a confining medium and provides confining pressure ($\sigma_2 = \sigma_3$) via 100 MPa precision piston pump. Axial stress (σ_1) is applied via a hydraulic intensifier/booster assembly that translates fluid pressure from a second syringe pump to a maximum stress of 680 MPa across a 40 mm sample diameter. As confining pressure increases to the target level, axial stress

is increased via digital servo control to maintain isostatic conditions. Once the desired environmental setting is achieved, the experiment begins with axial strain increased at a constant deformation rate of 3.6 mm/hr.

Axial displacement is measured with a non-contact eddy displacement system (EDS) attached to the apparatus. They are external to the pressure chamber and comprise of three sensors mounted to a lower fixed ring. The transducers accurately (sub-micron) record axial displacement by measuring the response from a target steel plate, which is attached to the top piston and responds with sample strain. Three readings are averaged and used to calculate strain, setting a target deformation rate via feedback to the axial stress intensifier. Strain values are subsequently corrected for machine stiffness (Fazio, 2017). Each sample was positioned inside an engineered rubber jacket fitted with ports where an array of twelve 1 MHz single-component Piezo-Electric Transducers (PZTs, model PAC Nano30) were embedded (e.g., Benson et al., 2007). These sensors have a relatively flat frequency response between 125 and 750 KHz. Sensor output is connected to preamplifiers (selectable between 30 and 70 dB) and split between two AE recorders. One output is used for continuous digitization, and a second recorder operates in a standard "triggered" mode which downloads all 12 channels when any single channel passes a set 100 mV threshold. Both systems used an amplification of 40 dB for the experiments presented here, which also include a band-pass filter of 50 kHz to 1 MHz to remove local noise which prioritized AE data quality over large numbers of events (Fazio et al., 2017); however, only the triggered mode data is used in this study. In addition to passive mode (recording fracture events across the array), the sensors may be used in "active" mode for P-wave elastic velocity measurements. To generate a survey, each sensor was triggered in sequence with a high voltage (200 V) pulse; the energy was recorded by the remaining 11 sensors in the array. Signal-to-noise was further improved by pulsing each sensor multiple times (16) and stacking the received waveforms, with each survey of 12-sensors generating 144 raypaths and taking ~30 s to complete. Velocity surveys were performed periodically through the experiment in order to derive velocity models for source location.

2.3. Computational Methods

The onset of recorded AE are picked automatically using a Distributed Time Delay Neural Network (King et al., 2020; Peddinti et al., 2015; Waibel et al., 1995). A model is trained on timeseries of instantaneous frequency (N. E. Huang et al., 1998), seismic amplitude and permutation entropy (Unakafova & Keller, 2013). By applying a simple binary classification to each AE signal, the waveform is categorized as either "background noise" or "signal." A simple time difference of arrival method (TDOA) is applied to locate the AE epicenters using the onset time of the "signal" classification (Comanducci et al., 2020; Tobias, 1976). Finally, pairwise subtraction of observed arrival times (a minimum of 6) to each sensor are minimized against calculated arrivals times through iterative estimation of the source location. The process is repeated until the location residual arrives to a local minimum, at the true source location.

Measurement of first motion polarity is as follows; each waveform of a located AE event is lowpass filtered to remove high frequency noise and the root mean square envelope is calculated (smoothing = 5). Starting from the onset of energy, the first motion is selected when amplitudes exceed 1.1 times the pre-signal noise and the signal begins to decrease in amplitude, thus targeting the first oscillation of the waveform. Polarity amplitudes for each event are then normalized to the maximum arrival amplitude of that event and projected onto a sphere (using a minimum of 8 measurements).

The objective of the following procedure is to minimize the fit between idealized focal spheres of tensile (T-type), shearing (S-type), and compaction (C-type) events and iterative rotation (azimuth and elevation) of measured values (Figure 1). Idealized spheres are segmented according to those of Finck et al. (2003), where T-type represents dominantly dilatational or mixed-mode fracturing, and S-type as a pure double-couple source. C-type mechanisms are considered as a compensated linear vector dipole or CLVD source. As the geometry of the radiation pattern is inverse to T-type, C-type events are considered to be dominantly compressional in this study.

The minimization constant is defined as the multiplication of the L2 norm of absolute polarity residuals (−1 or 1—Figure 1, top) and the L2 norm of deviatoric amplitude residuals (smoothed distribution—Figure 1, bottom). This value arrives to a minimum at the best-fitting orientation of measured polarities. This method is applied for each idealized sphere and the one with the lowest minimization constant is selected as the
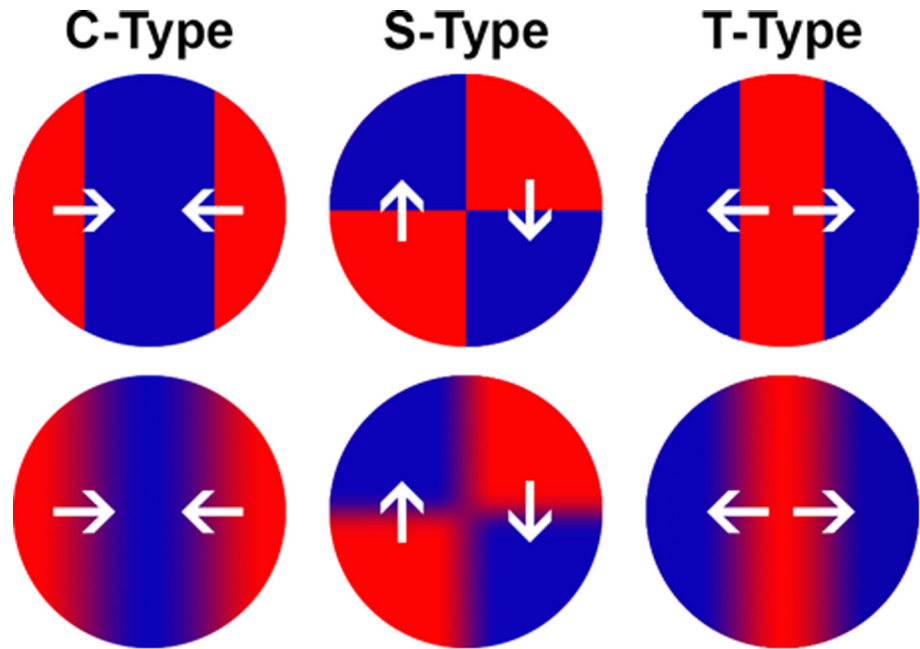
Figure 1. Absolute polarity (above) of idealized focal mechanisms of C-type (left), S-type (middle), and T-type (right) fracturing. Deviatoric amplitude distribution of the same mechanisms (below). White arrows indicate direction of motion from dilatant (red) to compactant (blue) regions.

true mechanism category. Slip planes are estimated from solved focal mechanisms. Estimated orientation of a focal "plane" is derived from the direction of motion. For C-type events, this is perpendicular to motion, whilst for S-type and T-type it is assumed parallel. Either plane may be selected for S-type events, however, under the compressive conditions of these experiments, normal (shear) faulting parallel to the shear direction is assumed.

This iterative method has some limitations. The first is associated to the choice of segmentation of the idealized focal spheres. Fracturing mechanisms fall within a range of distributions whose extremes are pure compaction, pure shear and pure tension (Frohlich et al., 2016). Unlike moment tensor inversion (e.g., Vavryčuk, 2005), our approach is limited to specific motions and is thus unable to precisely identify the amount of shear in a tensile event. Recent studies have highlighted the importance of regions of dilatancy and compaction in X-ray tomography during fault formation (Renard et al., 2019). By targeting specific fracturing mechanisms through the segmentation, variations of dilation and compaction in fracturing can be better studied. Attenuation or other scattering effects of the recorded waveforms are not accounted for here, which may affect the goodness of fit to the deviatoric mechanism (Vavryčuk, 2005). Furthermore, there is an increased uncertainty for events located above and below the sensing array due to poor azimuthal coverage of those events. As the majority of events are located in the center of the samples, where fracturing is generally diffuse, attenuation and scattering effects are considered to have a minimal impact on overall trends in the data.

To calculate the slip vectors, azimuthal directions are normalized according to the modal direction of S-type events for each experiment as these AE were principally orientated according to the dip direction of the fault zone. This allows to separate out events that dip parallel to the macroscopic failure plane from those that dip perpendicular to it. Given a dominance of shear faulting under compressive conditions, fracture azimuth and dip are assumed as slip vectors in order to calculate the divergence between neighboring events. Vector directions are interpolated onto a 3-D grid to identify general trends in stress orientation, after which the along-strike component is set to zero to calculate vector divergence as a 2-D plane (Figure 2).

For each mechanism category, a probability density function (PDF) is calculated for the time of occurrence of individual AE as a function of strain. Low-amplitude data are defined as AE with amplitudes in the bottom 5% of the total amplitude range for each mechanism of an experiment. All three PDFs are then summed
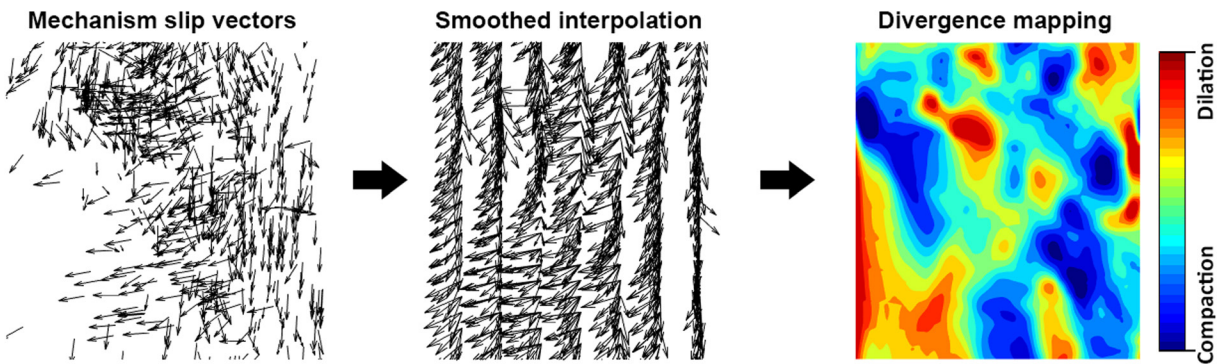
Figure 2. Slip vectors obtained from mechanism focal planes are first smoothed and interpolated onto a 3-D grid. The along strike component is set to zero and the divergence of this vector field is calculated to generate a 2-D map.

together, and a percentage contribution calculated. This approach was selected instead of histogram bins as it generates a smoother distribution and better highlights trends in the data. To ensure results are statistically relevant, the percentage trend is sampled once every 10 events for a particular experiment and then smoothed in a moving window of 0.04% strain. Results are split into three characteristic deformation stages that correlate with periods of: 1) fracture nucleation and fault growth (0%–70% UCS), 2) crack coalescence (70%–95% UCS), 3) dynamic failure of the sample (>95% UCS).

3. Results

Mechanical data highlight a progressive increase of peak strength with confining pressure that is observed for both lithologies (Figure 3). For confining pressures of 5, 10, 20, and 40 MPa, dynamic failure of Alzo Granite occurs at peak stresses of 175, 240, 325, and 475 MPa, respectively (Figure 3, left). Strain values at failure are 0.71%, 0.9%, 1.1%, and 1.45%, respectively. In each of the four experiments, an increase in AE is observed after a strain of ∼0.2%. For samples deformed at 5 and 10 MPa, an approximate exponential trend is seen in the counts of located AE after this point; however, for samples deformed at higher confining pressure (20 and 40 MPa), the increase in AE count is more linear, increasing to 100 and 200 counts respectively at peak stress. In all experiments the maximum AE output is seen to occur 0.1%–0.2% before failure, signifying a high number of microcracks during the yield stage of deformation, consistent with the timing of maximum AE observed in earlier work (Benson et al., 2019).

For DDS, dynamic failure of the sandstone samples occurs at peak stresses of 60, 110, 150, and 220 MPa for confining pressures of 5, 10, 20, and 40 MPa, respectively (Figure 3, right). The corresponding strain values at failure are 0.75%, 0.9%, 1.2%, and 1.3%. Unlike deformation in the Alzo Granite, failure of these samples is considerably more gradual with a less pronounced stress drop. As confining pressure increases, a longer period of strain softening (a slow decrease in differential stress as strain increases) is evident. In addition,
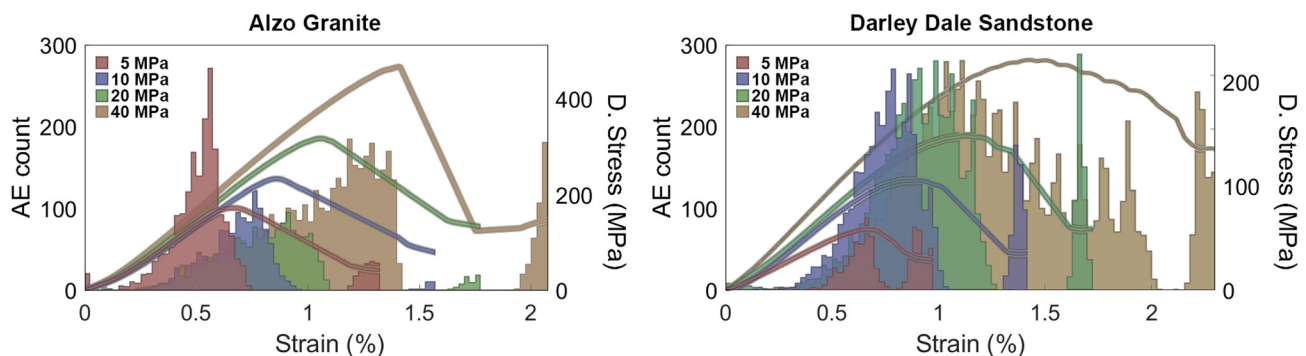

Figure 3. Stress-strain curves (line) and counts of located acoustic emission (AE, histogram) for Alzo Granite (left) and Darley Dale Sandstone (right) as samples are deformed.
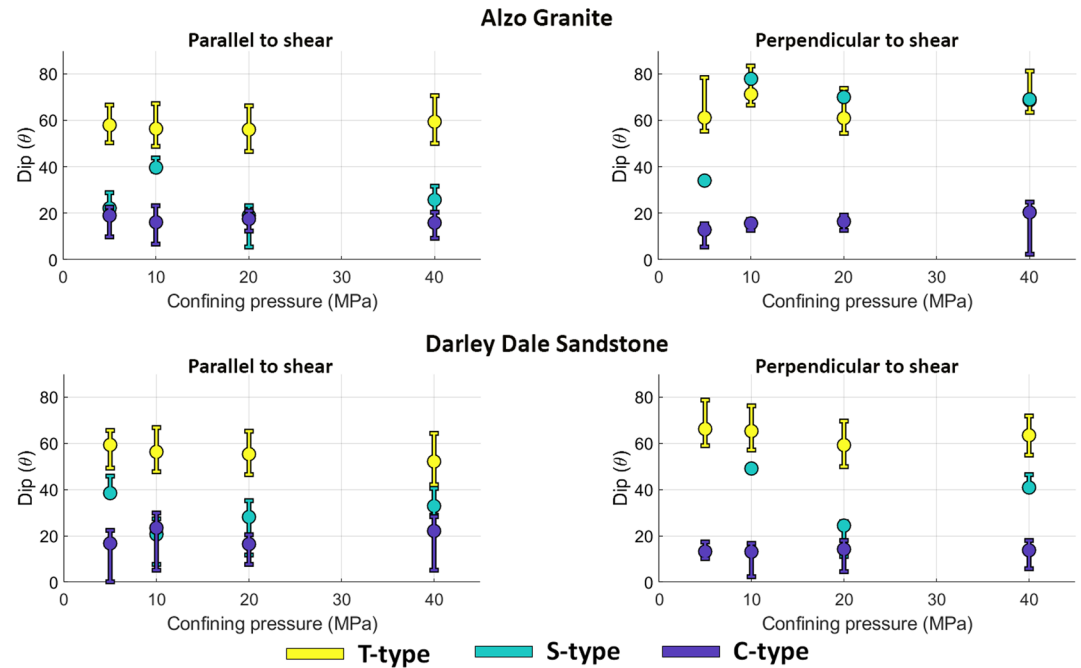
Figure 4. Average mechanism orientations are plotted against confining pressure for events dipping parallel or perpendicular to the sample failure plane. Error bars are defined as the standard error and represent the range of data from which the average is calculated.

the AE count rate always increases with increasing confining pressure from strains of ~0.5%. However, both the peak in AE count rate and the post-peak character show some changes with increasing confining pressure. The AE peak occurs close to the peak stress at lower confining pressure while it shifts to earlier times in the strain curve at higher confining pressures. In addition, the post-peak behavior is the same for stress and AE. Both show a quasi-ductile process, consistent with the smooth stress drop observed. A final burst of AE data after 0.9%, 1.2%, 1.6%, and 2.1% accompanies the final frictional sliding on the generated shear plane in each case, as also seen in the Alzo granite AE data.

3.1. Source Orientations and Location

AG and DDS demonstrate broadly similar trends in the relative distribution of fracturing mechanisms. Clear dominance of T-type fracturing is present at all confining pressures with typical counts 2–3 times larger than C-type fracturing. S-type fracturing occurs in very low numbers, although counts are larger in the sandstone than in the granite. Average orientations of fracture mechanisms are detailed in Figure 4 and compared with confining pressure. Circular points indicate the average of each of the mechanism types at the different confining pressures. Error bars are calculated as the standard deviation above and below the mean value and represent the spread of the data (Table 2).

For both rock types, T-type events are orientated generally perpendicular (dips higher than 60°) to the direction of principal stress, whilst C-type events show the opposite trend with sub-horizontal fracturing (dips less than 20°). S-type events are found across a range of dips between 20° and 60°. Although dip trends for all mechanisms are generally consistent as confining pressure increases, there is a notable rotation of shear-parallel T- and S-type in DDS that is consistent with previous observations of strain localization (e.g., Mair et al., 2002). At low confinements, deformation principally occurs in bands parallel to the main direction of compression. As stress increases, these bands develop a shear-component causing the angle between the most compressive direction and the band to increase (Bésuelle, 2001a, 2001b). However, this trend is not present in AG, where instead shear parallel T- and S-type follow opposed trends with shear perpendicular C-type events steepening as confining pressure increases.

Table 2
Counts of Solved Mechanisms of C-Type, S-Type, and T-Type Fracturing

Rock type	Pressure (MPa)	Parallel to shear			Perpendicular to shear		
		T-type	S-type	C-type	T-type	S-type	C-type
Alzo Granite	**5**	**1,103**	**64**	**325**	**489**	**11**	**252**
	10	705	45	109	390	8	132
	20	847	84	387	451	17	245
	40	2,353	283	813	1,113	12	293
Darley Dale Sandstone	5	440	22	198	151	0	58
	10	1,465	161	822	1,202	11	653
	20	**2,493**	**137**	**822**	**1,671**	**112**	**620**
	40	3,879	647	1,825	1,900	125	1,633

Note. Data are separated into groups that dip parallel or perpendicular to the principle shear direction. A dominance of T-type fracturing is observed for all samples, followed by C-type. Counts of S-type events are remarkably low for both rock types. Bold conditions and values have been chosen for analysis in Figures 5–9.

To analyze the time and spatial evolution of the source mechanisms with relation to the evolving mechanical steps, the following key periods are selected: 1) fracture nucleation and growth, 2) crack coalescence, and 3) dynamic failure. Mechanism orientations are first presented, then divergence maps are shown to highlight a simplified fracture pattern, and finally percentage mechanisms trends are shown for AG data collected at 5 MPa confining pressure and DDS data at 20 MPa. These were selected as they highlighted the most representative patterns observed in the formation and evolution of the fault zone (see supporting information for detail of experimental conditions).

Post-deformation imaging in AG at 5 MPa and DDS at 20 MPa (hereafter referred to as AG_5 and DDS_20) reveals relatively simple surface expressions of newly formed fracture structures (dashed red line—Figures 5a and 6a, respectively). Sample AG_5 (Figure 5c) demonstrates axial splitting in the form of T-type during the whole experiment: Characteristically steeply dipping (>60°) events with no clear preference in the dip direction or positioning (i.e., on- or off-fault, Aben et al., 2019). Two potential faults extending
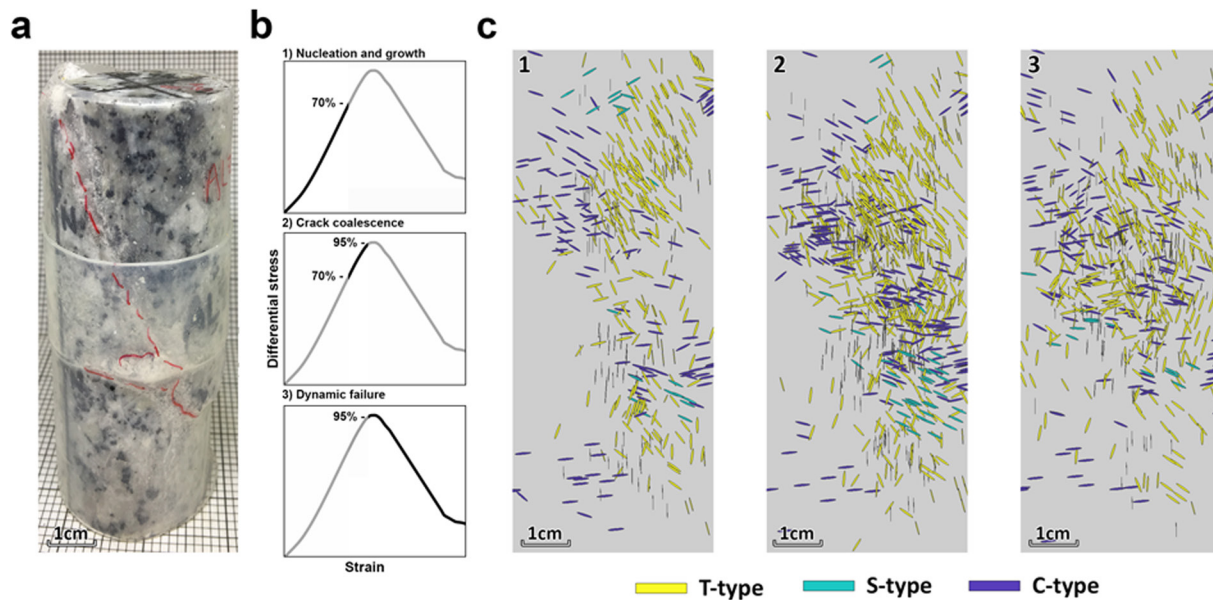

Figure 5. (a) Post-deformation photo of Alzo Granite deformed at 5 MPa. (b) Simple stress versus strain plots indicating time periods. (c) Spatial distribution of solved focal mechanisms in windows of 1) fracture nucleation and growth, 2) crack coalescence and 3) dynamic failure. Gray region indicates sample dimensions.

Figure 6. (a) Post-deformation photo of Darley Dale Sandstone deformed at 20 MPa. (b) Simple stress versus strain plots indicating time periods. (c) Spatial distribution of solved focal mechanisms in windows of 1) fracture nucleation and growth, 2) crack coalescence, and 3) dynamic failure. Gray region indicates sample dimensions.
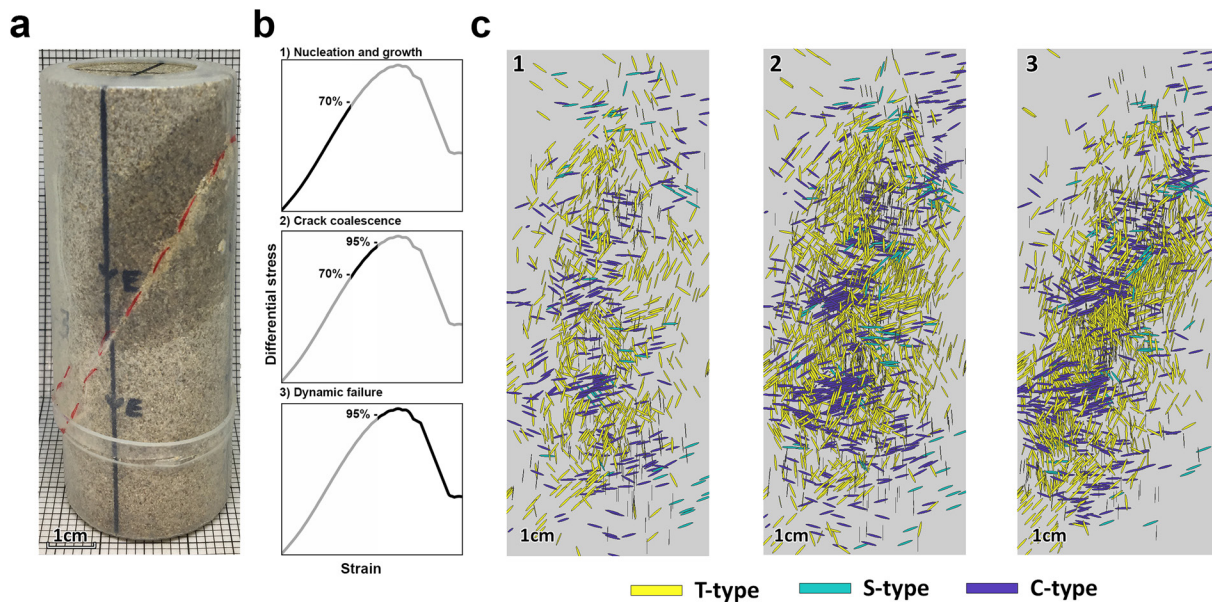
from the left corners are highlighted by the distribution of C-type fracturing during period 1. An increase in fault-parallel S-type events during period 2 identifies the eventual failure direction with C-type localizing along the failure plane. Following dynamic failure (period 3), fracturing events remain strongly diffuse throughout the sample.

Sample DDS_20 reveals an overall trend for strain localization, with more events attributed to the eventual failure plane as deformation progresses (Figure 6c). The event locations are diffused throughout the sample during the early stages of deformation. As strain increases, a leftward-dipping region of sub-horizontal C-type events precedes a bulk rotation of source locations (period 1). Like AG_5, two potential faults extending from the right-hand corners are visible. During crack coalescence (period 2) T-type events localize to both an upper cluster and a central 45°-dipping lineation. Following failure (period 3), C-type locations are consistent with the post-test imagery of the final fault (e.g., Benson et al., 2010; Lockner et al., 1992), with T-type fracturing occurring along a 45° band. S-type fracturing remains diffuse in the sample throughout the whole experiment. Although events dip in the same direction as the developing fault zone, source locations do not highlight how these events relate to the macro-structure.

3.2. Dilatancy Versus Compaction

In order to further investigate the competing mechanisms, divergence maps of mechanism slip vectors were derived (Figures 7 and 8**)**. An important distinction of these maps is that regions of compaction and dilatancy do not necessarily correlate with the distribution of C- and T-type mechanisms previously discussed. Similar to results obtained via 3-D X-Ray Tomography (Renard et al., 2019), they represent the general stress field of the samples as they undergo deformation and reveal how dislocations caused by the different fracture mechanisms interact with each other over longer distances (Zang & Stephansson, 2010). Due to the smoothing imposed by the interpolation (Figure 2) anomalies have a minimum dimension of ~1 cm.

A central rightward-dipping region of dilatancy characterizes the fault zone in AG_5 (Figure 7). The edges of the fault are delineated by strong compaction anomalies from the start of the experiment. This is either caused by expansion of the fault core interacting with broad dilation anomalies to the top right and bottom left of the sample, or due to real compaction along the edges of the fault zone. A strong dilation anomaly (Figure 7b, circled) in top left portion of the fault zone (period 1) is observed to compact and then propagate down and along the fault zone during periods 2 and 3.
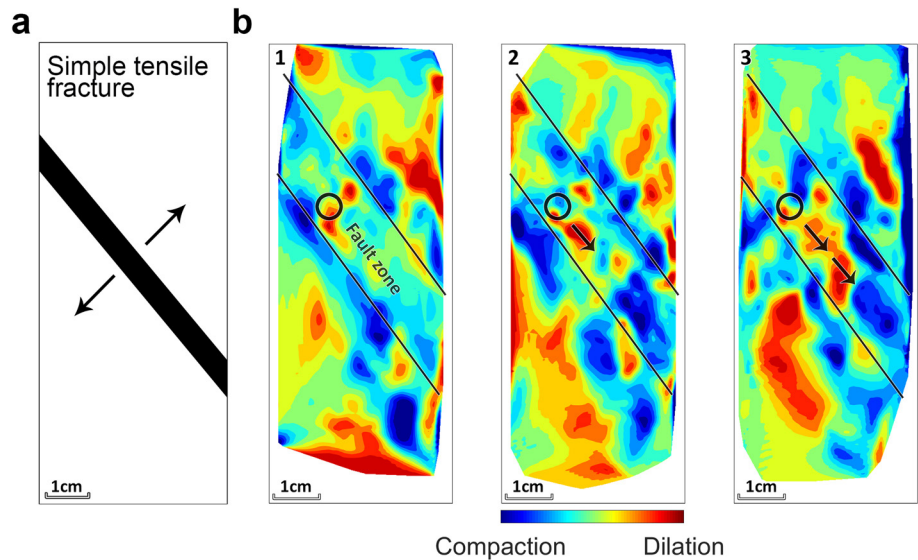
Figure 7. (a) Simplified fracture pattern in Alzo Granite deformed at 5 MPa. (b) Divergence maps of mechanism slip vectors. Red regions indicate dilatational regions where vector directions are diverging. Blue indicates compactant regions where vector directions are converging. Data are windowed into periods of 1) fracture nucleation and growth, 2) crack coalescence and 3) dynamic failure. Circles indicate a fracture nucleation point, whilst arrows highlight the direction of fracture propagation.

Unlike AG_5, which is characterized by a single fault throughout the test, DDS_20 demonstrates multiple, unrelated sources of dilatant fracturing (Figure 8b). Compaction follows a similarly broadly distributed trend delineating regions of sub-vertical dilation that may be analogous to the formation of axial splitting (period 1). As strain increases into period 2, anomalies are observed to connect into linear structures. Dilation anomalies not associated to this "connection" of structure also weaken, with some areas becoming dominated by compaction. However, these trends should be considered with caution as we do not consider
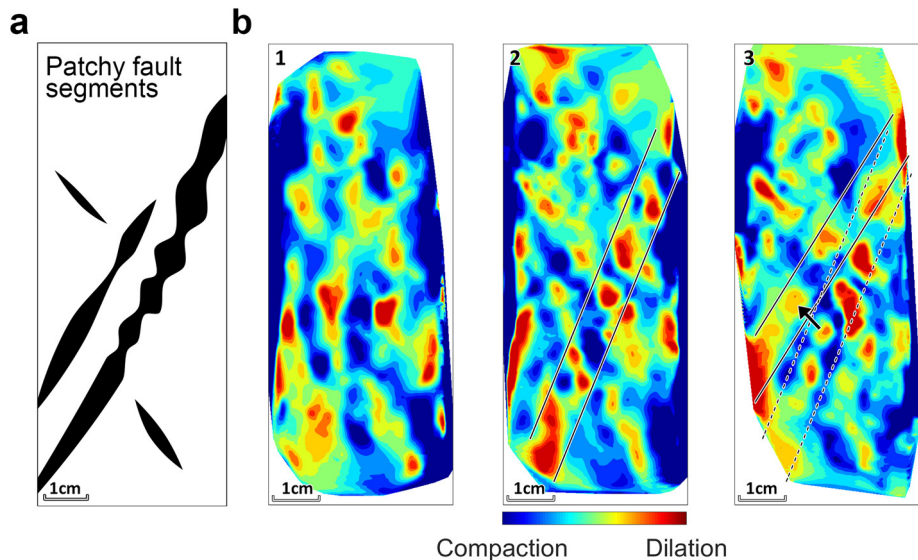

Figure 8. (a) Simplified fracture pattern for Darley Dale Sandstone deformed at 20 MPa. (b) Divergence maps of mechanism slip vectors. Red regions indicate dilatational regions where vector directions are diverging. Blue indicates compactant regions where vector directions are converging. Data are windowed into periods of 1) fracture nucleation and growth, 2) crack coalescence, and 3) dynamic failure. Rectangular regions and arrow highlight a switch in the dilating region during period 3.

the size of individual sources. A 60° lineation of dilatancy dominates the divergence field at this time, however, it is not entirely associated to observed failure structure in the post-test imagery (Figure 6a). Instead, dilation switches to a higher fault during dynamic failure of the sample with anomalies mainly extending from the top right to the bottom left (period 3).

Figures 7 and 10 reveal a relationship between regions of compaction and patchy dilatancy; however, the spatial mapping is insufficient to understand if they are antagonistic or in accordance. Percentage trends of the probability of fracturing mechanisms (Figure 9) highlight the variations in dominance of C-, S-, and T-type events as deformation progresses. The pattern of low-amplitude events (darker colors) reveals an underlying periodicity to the development of fracture structure where mechanisms transition in sequences. It is important to note that these are not a percentage of event counts, rather they are the percentage of the probability (or likelihood) of a specific mechanism occurring.

During period 1, high-amplitude C- and T-type fracturing are in accordance with each other for both samples. However, S-type events are more frequent in DDS_20 during this time than at later stages. At 0.3% and 0.45% strain (AG and DDS, respectively), there is a burst of low-amplitude T-type events that is related to the early axial splitting observed in the spatial mapping. This occurs before a periodic cycle of fracture development (period 2) during the elastic phase of deformation, where C-type events (0.4% and 0.65%) transition into S-type fractures (0.5% and 0.8%). The fractures peak at the start of crack coalescence before changing to T-type (0.6% and 0.95%). The antagonistic cycle between high-amplitude T- and C-type events (lighter colors, Figure 9) occurs once in AG_5 (strains of 0.3%–0.65%) and twice in DDS_20 (period 2%–0.6%–0.95%; period 3%–1%–1.3%). Unlike their high-amplitude events counterparts, there is no apparent antagonistic cycle between low-amplitude T- and C-type (darker color, Figure 9), suggesting that this only develops later during deformation. In both samples, dynamic failure is dominated by T-type fracturing with only a minor contribution of S-type.

4. Discussion

This study has analyzed fault zone development in Alzo Granite and DDS through characterization of individual AE source mechanisms using a modified first-motion polarity method. Data are broken up into characteristic periods of 1) fracture nucleation and growth, 2) crack coalescence, and 3) dynamic failure. This method differs from the average polarity approach (e.g., Stanchits et al., 2006) by projecting measurements onto idealized focal spheres. The advantage of this method is that it better accounts for the 3-D geometry of the source rather than assuming a dominance of either polarity to categorize events. A limitation is that results can be biased by the models used to fit the data. For instance, a looser definition of what marks a shear event would likely increase the number of events characterized here as S-type. Furthermore, tensile-shear (Liu et al., 2019) or compaction-shear (Bésuelle, 2001a, 2001b) events are likely to be marked as T- or C-type, respectively. Due to computational limitations it is unfeasible to address the full spectrum of fracturing types, nonetheless the results of this study demonstrate systematic variations in fracture development that can be attributed to the pre-existing conditions of the sample, that is, cohesive or granular, and the confining pressure applied during deformation.

The distribution of C-type fractures in Figure 5c shows that the failure plane nucleates at the edges of the sample (Benson et al., 2007) or is at least heavily influenced by them, with two potential faults visible in AG_5 during period 1. This observation implies that C-type events are an important precursor to crack coalescence. This is confirmed in DDS_20, where C-type fracturing dominates the failure plane throughout deformation (Figure 6c). Interestingly, there are isolated C-type events that are not associated to any prior fracturing, for instance in the top left of AG_5 in period 1 (Figure 5c). Within the sandstone this can be easily explained through mechanisms of pore collapse (Zhu et al., 2010), but this is unlikely in the granite, especially during the early stages of deformation. More likely, they represent a hybrid mode of compaction-tensile fracturing (CT-type). These low angle events form as part of a continuous transition between extension (tensile) and shear fracturing, and are thought to occur under mixed tensile and compressive stress conditions (Ramsey & Chester, 2004). In the Mount Desert Island Granite, stepped fracture geometry, consistent with fracture formation via linkage of en-echelon arrays, were identified as hybrid (CT) fractures
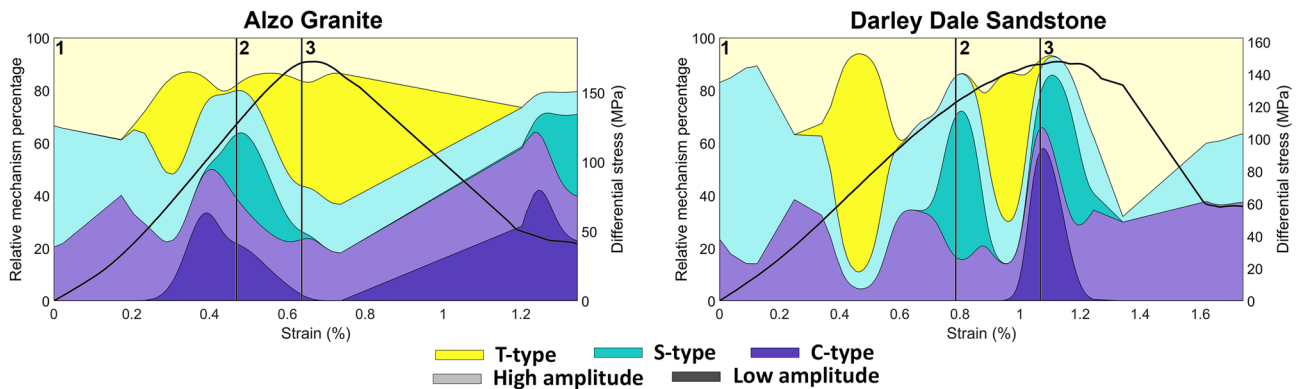
Figure 9. Mechanism percentage trends for Alzo Granite deformed at 5 MPa (left) and Darley Dale Sandstone deformed at 20 MPa (right). The changing dominance of T-type (yellow), S-type (green), and C-type (blue) events separated by amplitude (lighter for high, darker for low) is observed as strain increases. Data are windowed into periods of 1) fracture nucleation and growth, 2) crack coalescence, and 3) dynamic failure.

(Engelder, 1989, 1999). The results reported in this study suggest that CT-type events form during the earliest stages of fault zone formation (i.e., period 1) before any larger scale structure dominates the stress field.

A steepening of S-type and a shallowing of T-type events with increasing confining pressure in Figure 4 represents a switch from axial splitting to fault plane localization in DDS (Mair et al., 2002; Passelègue et al., 2016). AG demonstrates the opposite trend where S-type events become shallower and T-type steepen. Furthermore, there is a steepening of C-type events in the perpendicular direction. It is likely that these rotations occur as a result of the same transitionary switch present in DDS. However in samples of granite, X-ray tomography reveals that crack growth can be hampered by minerals and grain boundaries leading to closure near to the fracture tip (McBeck et al., 2019). In the case of AG, the presence of large feldspar grains can inhibit the propagation of S-type events (Yu et al., 2018; Zhao et al., 2019). Instead, these events will occur as C-type with fracturing developing perpendicular to the direction of shear. This shear inhibition will further reflect on shear-parallel T-type events, raising the average dip as more events become localized along the failure plane at higher confining pressures. This is consistent with the observation that the strength of a material dictates how and where a fracture will propagate (McBeck et al., 2017).

The presence of single or multi-periodic fracture growth in AG_5 and DDS_20, respectively (Figure 9), is likely related to the initial patchiness of dilatant regions. These cycles begin as a dominance of C- and S-type fracturing before transitioning to bursts of T-type events. This double-yielding behavior has been previously seen in triaxially compressed porous limestone (L. Huang et al., 2019). The authors observed cataclastic pore collapse, driven by shear enhanced compaction, preceding the development of widespread bifurcation. In AG_5, the end of this sequence results in dynamic failure of the sample, whilst in DDS_20 the cycle occurs twice. When an earthquake ruptures, it is likely to trigger an event on an adjacent fault due to perturbations of the local stress field (Wesnousky, 2006). As a result, clustered fractures are more likely to propagate than dispersed structure (McBeck et al., 2019). The mechanism divergence maps for AG_5 suggest that failure occurred due to the rupture of a single region of dilatancy in period 2 (Figure 7b). However, the dispersed structure of DDS_20 required an initial growth cycle to first align fracture segments before a second cycle resulted in sample failure (Figures 8b and 9, right).

Laboratory and numerical studies highlight creep patches or deformable bodies that occur prior to fault coalescence (e.g., Aldam et al., 2017; Kaneko & Lapusta, 2008). This has been interpreted to be analogous to foreshock sequences prior to a main shock earthquake (Kato et al., 2012; Latour et al., 2013). A meta-study on the occurrence of foreshocks debated their existence as either the result of tectonic loading or that they may reflect a triggering/excitation process (Mignan, 2014). The author concluded that this could only be resolved through large data sets that included significant amounts of microseismicity due to biases imposed by data selection. In Figure 9, the occurrence of low amplitude C- and S-type events prior to bursts of T-type activity leading to planar localization well represents the premonitory phase, or foreshock, before a critical damage threshold would allow the coalescence into a larger scale deformation structure.
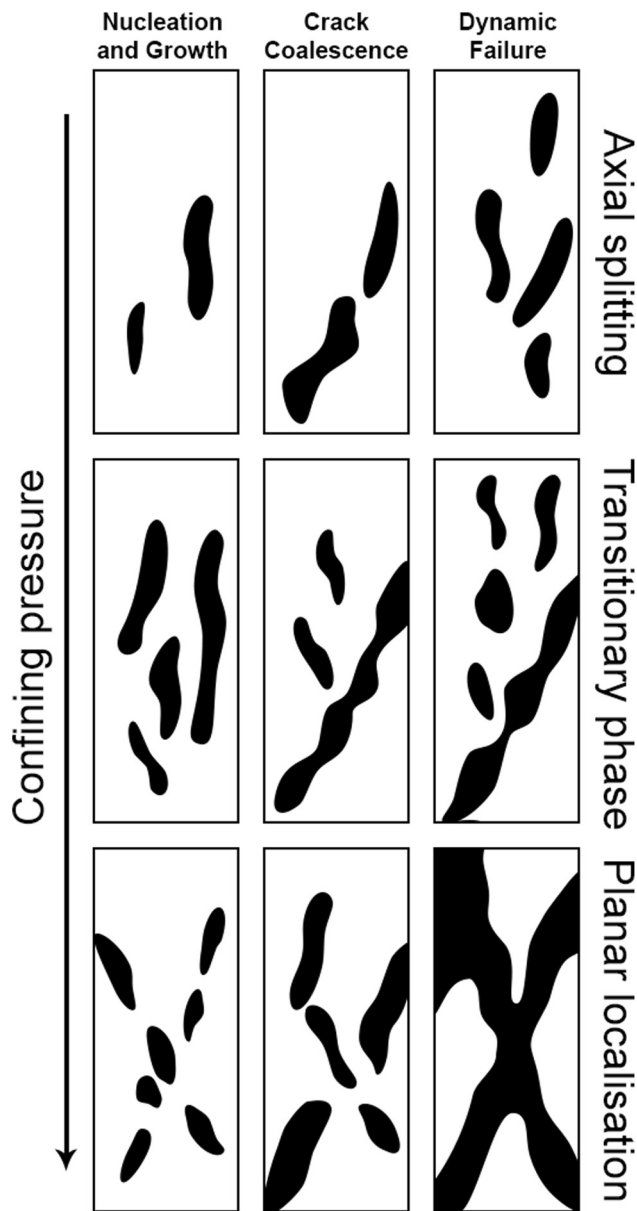
Figure 10. Simplified brittle failure patterns. Dilatant regions (black) highlight the changing distribution of deformation structure as confining pressure increases for the different deformation stages. A transitionary phase between axial splitting is identified where zones of deformation form into planar structure during crack coalescence.

In samples of Westerly Granite, Passelègue et al. (2016) identified transitionary phases between axial splitting at low pressures to shear localization at higher confinement as the sample fails. The mechanism divergence maps of all the analyzed pressures support this observation (see supporting information for all experimental conditions) and are summarized in Figure 10 as simplified brittle failure patterns. At low pressures the fracture energy of a fault is similar to that of minerals (Passelegue et al., 2016), where small asperities throughout the sample can accommodate strain resulting in a diffuse pattern of dilatancy. Under higher stress conditions the energy required to propagate a fracture is much larger, so only flaws that are preferentially aligned to the internal stress field will rupture. The samples analyzed here were undamaged at the start of deformation, therefore the alignment of easy-to-rupture flaws will be unlikely. At transitionary pressures, it is only when the concentration of dilatant regions reaches a threshold that axial splitting switches to localization (e.g., period 2 in DDS_20—Figure 8b). During period 1 and once confining pressures are sufficiently high, long-range elastic interactions between flaws in the sample allow for failure plane structures to localize earlier (Kandula et al., 2019).

5. Conclusions

The aim of this study was to identify patterns in the fracture development process by mapping rupture source mechanisms (tensile, shear, and collapse) derived from microseismic signatures (AE) recorded during conventional triaxial deformation experiments. Two lithologies, representing end members in terms of rock physical properties (e.g., fabric, porosity, grain size, and cementation), were used: Alzo Granite (AG), Italy and DDS (DDS), United Kingdom. Unlike the commonly used average polarity method (e.g., Stanchits et al., 2006) the approach reported here uses the source radiation pattern (Kwiatek & Ben-Zion, 2013) to categorize events and obtain source orientations of mixed-mode type mechanisms.

AE data from conventional triaxial compression tests of Alzo Granite and DDS at confining pressures of 5–40 MPa were investigated to identify evolving damage mechanisms process by mapping rupture source mechanisms using a least squares minimization of the 3-D focal sphere to classify fracturing mechanisms as tensile, shear or compaction. Results highlight a complex interplay between compactant (C-type) and dilatant (T-type) fracturing processes leading to the formation of the fault zone that is consistent in both lithologies. C-type events are the earliest precursor, identifying initial fault planes during crack nucleation. Low amplitude T-type events mark new cracks opening and the onset of fracture growth. This period of deformation induced fracture growth is characterized by periodic cycles of coalescence, transitioning from C- to shear (S-type) and then back to T-type events. At the end of each sequence, macroscopic structure forms. For Alzo Granite, a single damage cycle is sufficient to develop the planar localization leading to dynamic failure. Whilst in DDS it can take multiple cycles for coalescence to take place due to interacting mechanisms induced by multiple fracture nucleation sites.

The results of this study can have several implications for the interpretation of natural earthquakes precursors. The occurrence of C- and S-type events prior to bursts of T-type activity leading to planar localization well represents the premonitory phase, or foreshock, before a critical damage threshold would allow the coalescence into a larger scale deformation structure. Results also provide new insights for developing new

monitoring strategies for earthquake precursory detection. The identification of C- and S- type events could provide an early warning signature before premonitory slip occurs.

Data Availability Statement

Acoustic emission data are obtained at the Rock Mechanics Laboratory, University of Portsmouth. Due to the size of the data sets, acoustic emission are unavailable. Programming codes were developed in MAT-LAB® version 2018a and are available at https://zenodo.org/record/4059413#.X3Rhx4xfhPY.

References

Aben, F. M., Brantut, N., Mitchell, T. M., & David, E. C. (2019). Rupture energetics in crustal rock from laboratory-scale seismic tomography. *Geophysical Research Letters*, *46*, 7337–7344. https://doi.org/10.1029/2019gl083040

Aldam, M., Weikamp, M., Spatschek, R., Brener, E. A., & Bouchbinder, E. (2017). Critical nucleation length for accelerating frictional slip. *Geophysical Research Letters*, *44*, 11390–11398. https://doi.org/10.1002/2017gl074939

Ashby, M. F., & Hallam, S. D. (1986). The failure of brittle solids containing small cracks under compressive stress states. *Acta Metallurgica*, *34*, 497–510. https://doi.org/10.1016/0001-6160(86)90086-6

Baud, P., & Meredith, P. (1997). Damage accumulation during triaxial creep of Darley Dale sandstone from pore volumometry and acoustic emission. *International Journal of Rock Mechanics and Mining Sciences*, *34*(3–4), 24.e1–24.e10. https://doi.org/10.1016/s1365-1609(97)00060-9

Baud, P., Wong, T.-f., & Zhu, W. (2014). Effects of porosity and crack density on the compressive strength of rocks. *International Journal of Rock Mechanics and Mining Sciences*, *67*, 202–211. https://doi.org/10.1016/j.ijrmms.2013.08.031

Benson, P. M., Austria, D. C., Gehne, S., Butcher, E., Harnett, C. E., Fazio, M., et al. (2019). Laboratory simulations of fluid-induced seismicity, hydraulic fracture, and fluid flow. *Geomechanics of Energy and the Environment*, *24*, 100169. https://doi.org/10.1016/j.gete.2019.100169

Benson, P. M., Thompson, B. D., Meredith, P. G., Vinciguerra, S., & Young, R. P. (2007). Imaging slow failure in triaxially deformed Etna basalt using 3D acoustic-emission location and X-ray computed tomography. *Geophysical Research Letters*, *34*, L03303. https://doi.org/10.1029/2006gl028721

Benson, P. M., Vinciguerra, S., Meredith, P. G., & Young, R. P. (2010). Spatio-temporal evolution of volcano seismicity: A laboratory study. *Earth and Planetary Science Letters*, *297*, 315–323. https://doi.org/10.1016/j.epsl.2010.06.033

Bésuelle, P. (2001a). Compacting and dilating shear bands in porous rock: Theoretical and experimental conditions. *Journal of Geophysical Research*, *106*, 13435–13442. https://doi.org/10.1029/2001jb900011

Bésuelle, P. (2001b). Evolution of strain localization with stress in a sandstone: Brittle and semi-brittle regimes. *Physics and Chemistry of the Earth*, *26*, 101–106. https://doi.org/10.1016/s1464-1895(01)00032-1

Bugini, R., Pavese, A., Borroni, S., & Folli, L. (2000). *White granites used in Lombard architecture*. In Proceedings of the 9th International Congress on Deterioration and Conservation of Stone (pp. 41–48), Elsevier. https://doi.org/10.1016/B978-044450517-0/50084-2

Cavallo, A., Bigioggero, B., Colombo, A., & Tunesi, A. (2004). The Verbano Cusio Ossola province: A land of quarries in northern Italy (Piedmont). *Miner*, *73*, 197.

Chen, H. K., Zhou, Y. T., & Wang, Z. (2014). Study on damage characteristics of unstable rocks under excitation effect. In *Applied mechanics and materials* (pp. 575–581), Trans Tech Publications.

Comanducci, L., Cobos, M., Antonacci, F., & Sarti, A. (2020). *Time difference of arrival estimation from frequency-sliding generalized cross-correlations using convolutional neural networks*. In 2020 IEEE International Conference on Acoustics, Speech and Signal Processing (ICASSP), Barcelona, Spain. https://doi.org/10.1109/icassp40776.2020.9053429

Cox, S. J. D., & Scholz, C. H. (1988). Rupture initiation in shear fracture of rocks: An experimental study. *Journal of Geophysical Research*, *93*, 3307–3320. https://doi.org/10.1029/jb093ib04p03307

Engelder, T. (1989). Analysis of pinnate joints in the Mount Desert Island granite: Implications for postintrusion kinematics in the coastal volcanic belt, Maine. *Geologica*, *17*, 564–567. https://doi.org/10.1130/0091-7613(1989)017<0564:aopjit>2.3.co;2

Engelder, T. (1999). Transitional-tensile fracture propagation: A status report. *Journal of Structural Geology*, *21*, 1049–1055. https://doi.org/10.1016/s0191-8141(99)00023-1

Fazio, M. (2017). *Dynamic laboratory simulations of fluid-rock coupling with application to volcano seismicity and unrest (PhD Thesis)*. University of Portsmouth, School of Earth and Environmental Sciences.

Fazio, M., Benson, P. M., & Vinciguerra, S. (2017). On the generation mechanisms of fluid-driven seismic signals related to volcano-tectonics. *Geophysical Research Letters*, *44*, 734–742. https://doi.org/10.1002/2016gl070919

Finck, F., Yamanouchi, M., Reinhardt, H.-W., & Grosse, C. U. (2003). Evaluation of mode I failure of concrete in a splitting test using acoustic emission technique. *International Journal of Fracture*, *124*, 139–152. https://doi.org/10.1023/b:frac.0000018234.61956.ff

Frohlich, C., DeShon, H., Stump, B., Hayward, C., Hornbach, M., & Walter, J. I. (2016). A historical review of induced earthquakes in Texas. *Seismological Research Letters*, *87*, 1022–1038. https://doi.org/10.1785/0220160016

Hanks, T. C. (1992). Small earthquakes, tectonic forces. *Science*, *256*, 1430–1432. https://doi.org/10.1126/science.256.5062.1430

Hatton, C. G., Main, I. G., & Meredith, P. G. (1994). Non-universal scaling of fracture length and opening displacement. *Nature*, *367*, 160–162. https://doi.org/10.1038/367160a0

Healy, D., Jones, R. R., & Holdsworth, R. E. (2006). Three-dimensional brittle shear fracturing by tensile crack interaction. *Nature*, *439*, 64–67. https://doi.org/10.1038/nature04346

Heap, M. J., Baud, P., Meredith, P. G., Bell, A. F., & Main, I. G. (2009). Time-dependent brittle creep in Darley Dale sandstone. *Journal of Geophysical Research*, *114*, B07203. https://doi.org/10.1029/2008jb006212

Huang, L., Baud, P., Cordonnier, B., Renard, F., Liu, L., & Wong, T.-F. (2019). Synchrotron X-ray imaging in 4D: Multiscale failure and compaction localization in triaxially compressed porous limestone. *Earth and Planetary Science Letters*, *528*, 115831. https://doi.org/10.1016/j.epsl.2019.115831

Huang, N. E., Shen, Z., Long, S. R., Wu, M. C., Shih, H. H., Zheng, Q., et al. (1998). The empirical mode decomposition and the Hilbert spectrum for nonlinear and non-stationary time series analysis. *Proceedings of the Royal Society of London A*, *454*, 903–995. https://doi.org/10.1098/rspa.1998.0193

Hudson, J. A., Kennett, B. L. N., Richards, P. G., & Freeman, W. H. (1981). Quantitative seismology (two vols) K. Aki and P. G. Richards, W. H. Freeman, San Francisco 934 pp. $35.00 (£20.70 per volume). *Geophysical Journal International*, *64*, 802–806. https://doi.org/10.1093/gji/64.3.802

Kádár, V., Pál, G., & Kun, F. (2020). Record statistics of bursts signals the onset of acceleration towards failure. *Scientific Reports*, *10*, 1–12. https://doi.org/10.1038/s41598-020-59333-4

Kandula, N., Cordonnier, B., Boller, E., Weiss, J., Dysthe, D. K., & Renard, F. (2019). Dynamics of microscale precursors during brittle compressive failure in Carrara marble. *Journal of Geophysical Research: Solid Earth*, *124*, 6121–6139. https://doi.org/10.1029/2019jb017381

Kaneko, Y., & Lapusta, N. (2008). Variability of earthquake nucleation in continuum models of rate-and-state faults and implications for aftershock rates. *Journal of Geophysical Research*, *113*, B12312. https://doi.org/10.1029/2007jb005154

Kato, A., Obara, K., Igarashi, T., Tsuruoka, H., Nakagawa, S., & Hirata, N. (2012). Propagation of slow slip leading up to the 2011 Mw 9.0 Tohoku-Oki earthquake. *Science*, *335*, 705–708. https://doi.org/10.1126/science.1215141

Kemeny, J. M., & Cook, N. G. (1991). *Micromechanics of deformation in rocks*. In *Toughening mechanisms in quasi-brittle materials* (pp. 155–188), Springer.

King, T., Benson, P., De Siena, L., & Vinciguerra, S. (2020). Acoustic emission waveform picking with time delay neural networks during rock deformation laboratory experiments. *Seismological Research Letters*, *92*, 923–932.

Kwiatek, G., & Ben-Zion, Y. (2013). Assessment of PandSwave energy radiated from very small shear-tensile seismic events in a deep South African mine. *Journal of Geophysical Research: Solid Earth*, *118*, 3630–3641. https://doi.org/10.1002/jgrb.50274

Latour, S., Schubnel, A., Nielsen, S., Madariaga, R., & Vinciguerra, S. (2013). Characterization of nucleation during laboratory earthquakes. *Geophysical Research Letters*, *40*, 5064–5069. https://doi.org/10.1002/grl.50974

Lei, X., Kusunose, K., Rao, M. V. M. S., Nishizawa, O., & Satoh, T. (2000). Quasi-static fault growth and cracking in homogeneous brittle rock under triaxial compression using acoustic emission monitoring. *Journal of Geophysical Research*, *105*, 6127–6139. https://doi.org/10.1029/1999jb900385

Lei, X., Nishizawa, O., Kusunose, K., & Satoh, T. (1992). Fractal structure of the hypocenter distributions and focal mechanism solutions of acoustic emission in two granites of different grain sizes. *Journal of Physics of the Earth*, *40*, 617–634. https://doi.org/10.4294/jpe1952.40.617

Liu, W., Liu, Y., Du, Y., Pang, L., & Meng, X. (2019). Study on the development and distribution rule of tensile shear fracture propagation angle of fractured rock mass under seepage pressure. *Geotechnical & Geological Engineering*, *37*, 4151–4161. https://doi.org/10.1007/s10706-019-00899-w

Lockner, D. A., Byerlee, J. D., Kuksenko, V., Ponomarev, A., & Sidorin, A. (1992). Observations of quasistatic fault growth from acoustic emissions. In *International geophysics* (pp. 3–31), Elsevier.

Mair, K., Elphick, S., & Main, I. (2002). Influence of confining pressure on the mechanical and structural evolution of laboratory deformation bands. *Geophysical Research Letters*, *29*, 49–51. https://doi.org/10.1029/2001gl013964

McBeck, J., Cooke, M., & Madden, E. (2017). Work optimization predicts the evolution of extensional step overs within anisotropic host rock: Implications for the San Pablo Bay, CA. *Tectonics*, *36*, 2630–2646. https://doi.org/10.1002/2017tc004782

McBeck, J., Kandula, N., Aiken, J. M., Cordonnier, B., & Renard, F. (2019). Isolating the factors that govern fracture development in rocks throughout dynamic in situ X-ray tomography experiments. *Geophysical Research Letters*, *46*(20), 11127–11135. https://doi.org/10.1029/2019GL084613

McClintock, F. A. (1962). *Friction on Griffith cracks in rocks under pressure*. In Proceedings of the Fourth U.S. National Congress of Applied Mechanics, pp. 1015–1022.

Mignan, A. (2014). The debate on the prognostic value of earthquake foreshocks: A meta-analysis. *Scientific Reports*, *4*, 4099. https://doi.org/10.1038/srep04099

Passelègue, F. X., Schubnel, A., Nielsen, S., Bhat, H. S., Deldicque, D., & Madariaga, R. (2016). Dynamic rupture processes inferred from laboratory microearthquakes. *Journal of Geophysical Research: Solid Earth*, *121*, 4343–4365. https://doi.org/10.1002/2015jb012694

Peddinti, V., Chen, G., Manohar, V., Ko, T., Povey, D., & Khudanpur, S. (2015). *JHU ASpIRE system: Robust LVCSR with TDNNS, iVector adaptation and RNN-LMS*. In 2015 IEEE Workshop on Automatic Speech Recognition and Understanding (ASRU) (pp. 539–546), IEEE.

Ramsey, J. M., & Chester, F. M. (2004). Hybrid fracture and the transition from extension fracture to shear fracture. *Nature*, *428*, 63–66. https://doi.org/10.1038/nature02333

Renard, F., McBeck, J., Kandula, N., Cordonnier, B., Meakin, P., & Ben-Zion, Y. (2019). Volumetric and shear processes in crystalline rock approaching faulting. *Proceedings of the National Academy of Sciences of the United States of America*, *116*, 16234–16239. https://doi.org/10.1073/pnas.1902994116

Stanchits, S., Vinciguerra, S., & Dresen, G. (2006). Ultrasonic velocities, acoustic emission characteristics and crack damage of basalt and granite. *Pure and Applied Geophysics*, *163*, 975–994. https://doi.org/10.1007/s00024-006-0059-5

Tobias, A. (1976). Acoustic-emission source location in two dimensions by an array of three sensors. *Non-Destructive Testing*, *9*, 9–12. https://doi.org/10.1016/0029-1021(76)90027-x

Unakafova, V., & Keller, K. (2013). Efficiently measuring complexity on the basis of real-world data. *Entropy*, *15*, 4392–4415. https://doi.org/10.3390/e15104392

Vavryčuk, V. (2005). Focal mechanisms in anisotropic media. *Geophysical Journal International*, *161*, 334–346.

Waibel, A., Hanazawa, T., Hinton, G., Shikano, K., & Lang, K. J. (1995). Phoneme recognition using time-delay neural networks. *Backpropagation Theory Architecture Application*, *37*, 328–339.

Wesnousky, S. G. (2006). Predicting the endpoints of earthquake ruptures. *Nature*, *444*, 358–360. https://doi.org/10.1038/nature05275

Yu, M., Wei, C., Niu, L., Li, S., & Yu, Y. (2018). Calculation for tensile strength and fracture toughness of granite with three kinds of grain sizes using three-point-bending test. *PLoS One*, *13*, e0180880. https://doi.org/10.1371/journal.pone.0180880

Zang, A., Christian Wagner, F., Stanchits, S., Dresen, G., Andresen, R., & Haidekker, M. A. (1998). Source analysis of acoustic emissions in Aue granite cores under symmetric and asymmetric compressive loads. *Geophysical Journal International*, *135*, 1113–1130. https://doi.org/10.1046/j.1365-246x.1998.00706.x

Zang, A., & Stephansson, O. (2010). Rock fracture criteria. In *Stress field of the Earth's crust* (pp. 37–62), Springer.

Zhao, D., Zhang, S., & Wang, M. (2019). *Microcrack growth properties of granite under ultrasonic high-frequency excitation* [WWW Document]. Advances in Civil Engineering. https://doi.org/10.1155/2019/3069029

Zhu, W., Baud, P., & Wong, T. (2010). Micromechanics of cataclastic pore collapse in limestone. *Journal of Geophysical Research*, *115*, B04405. https://doi.org/10.1029/2009jb006610

Zhu, W., & Wong, T.-F. (1997). The transition from brittle faulting to cataclastic flow: Permeability evolution. *Journal of Geophysical Research*, *102*, 3027–3041. https://doi.org/10.1029/96jb03282